EPRI | ELECTRIC POWER RESEARCH INSTITUTE

Mitigation of Explosive Cleaning Damage in 300 Series Stainless Steels

Interim Report

1022240

Mitigation of Explosive Cleaning Damage in 300 Series Stainless Steels

Interim Report

1022240

Technical Update, March 2011

EPRI Project Manager

D. Glanton

ELECTRIC POWER RESEARCH INSTITUTE
3420 Hillview Avenue, Palo Alto, California 94304-1338 ▪ PO Box 10412, Palo Alto, California 94303-0813 ▪ USA
800.313.3774 ▪ 650.855.2121 ▪ askepri@epri.com ▪ www.epri.com

DISCLAIMER OF WARRANTIES AND LIMITATION OF LIABILITIES

THE FOLLOWING ORGANIZATION(S), UNDER CONTRACT TO EPRI, PREPARED THIS REPORT:

Colorado School of Mines

Xcel Energy

Electric Power Research Institute (EPRI)

This is an EPRI Technical Update report. A Technical Update report is intended as an informal report of continuing research, a meeting, or a topical study. It is not a final EPRI technical report.

NOTE

For further information about EPRI, call the EPRI Customer Assistance Center at 800.313.3774 or e-mail askepri@epri.com.

ACKNOWLEDGMENTS

The following organization(s), under contract to the Electric Power Research Institute (EPRI), prepared this report:

Colorado School of Mines
1500 Illinois St.
Golden, CO 80401

Principal Investigator
S. Liu

Xcel Energy
414 Nicollet Mall
Minneapolis, MN 55401

Principal Investigator
R. Hellner

Electric Power Research Institute
1300 West W.T. Harris Blvd.
Charlotte, NC 28262

This report describes research sponsored by EPRI.

This publication is a corporate document that should be cited in the literature in the following manner:

Mitigation of Explosive Cleaning Damage in 300 Series Stainless Steels: Interim Report. EPRI, Palo Alto, CA: 2011. 1022240.

PRODUCT DESCRIPTION

Results and Findings

This report describes the aging and damage mechanisms in austenitic stainless steel as they relate to explosive cleaning of boiler tubing. By understanding the interaction between the damage and aging mechanisms, optimal blasting parameters can be defined.

Challenges and Objectives

The purpose of the project described in this report is to understand and characterize the damage mechanisms that lead to explosive cleaning damage in austenitic boiler tubes. The project will publish guidelines regarding ways to minimize or eliminate damage resulting from explosive cleaning.

Applications, Value, and Use

The mitigation of explosive cleaning damage will greatly reduce the risk of forced outage time resulting from boiler tube damage, which might not always be apparent on the surface of a blasted tube. In addition, optimal blasting parameters will prevent reductions in boiler tube life resulting from explosive cleaning damage.

EPRI Perspective

As more fossil-fired units shift toward the use of Powder River Basin (PRB) coal, boiler tube slag removal becomes increasingly difficult. Explosive cleaning is a possible solution to this problem of strongly adherent slag. However, explosive cleaning damage and explosive cleaning optimal parameters have not been well understood. The Electric Power Research Institute (EPRI) is in a unique position to leverage its members' boiler tube blasting experiences to mitigate explosive cleaning damage.

Approach

The goals of this report are to understand the mechanisms of explosive cleaning damage and how they are affected by aging of boiler tubes. These goals were accomplished by examining aging embrittlement phenomena and by simulating explosive cleaning damage in boiler tubing.

Keywords

Austenitic tubing
Blasting
Boiler tube
Dynamite
Explosive cleaning
Slag removal

CONTENTS

LIST OF FIGURES

LIST OF TABLES

1
INTRODUCTION

Boiler slagging, that is the buildup of iron or silicate-rich ash deposits, on heat exchanger tubes in coal fired power plants has been a major problem resulting in the loss of millions of dollars annually due to decreased efficiency. Ash forms as a result of combustion and gasification of inorganic materials and solidifies as submicron sized particles upon cooling. Coalescence of these particles with time leads to the formation of thick layers of slags on the boiler tubes. Conventional slag removal methods include soot blowers and water lance cleaning devices. These techniques are only partially successful in removing deposits from the downstream side of heat transfer tube bundles. Another technique is used with more success: detonation waves. While the traveling shock wave created by explosive detonation may result in a more convenient, inexpensive, and effective method of slag removal, the effects of traveling shock waves on the heat exchanger tubes are not entirely understood.

1.1 Explosive Cleaning Process

Explosive cleaning is a process by which power utilities remove coal ash (slag) from industrial coal-fired boilers by detonating a suitable explosive near slag covered boiler tubes. A photograph of slag covered boiler tubes is shown in Figure 1-1. Austenitic stainless steel tubes are commonly used in sections of a boiler. During the explosive cleaning process the tubes undergo a stress pulse that propagates through the tube as shown in Figure 1-2. A typical dynamite blast has two to three compressive pulses but because the geometry of a tube allows for the superposition of the pulses, tensile stresses are generated at specific locations throughout the tube. Each of these individual pulses represents one loading cycle that may contribute to the overall cumulative deformation in time leading to fatigue.

Figure 1-1
Boiler tubes covered in coal ash (slag). [1]

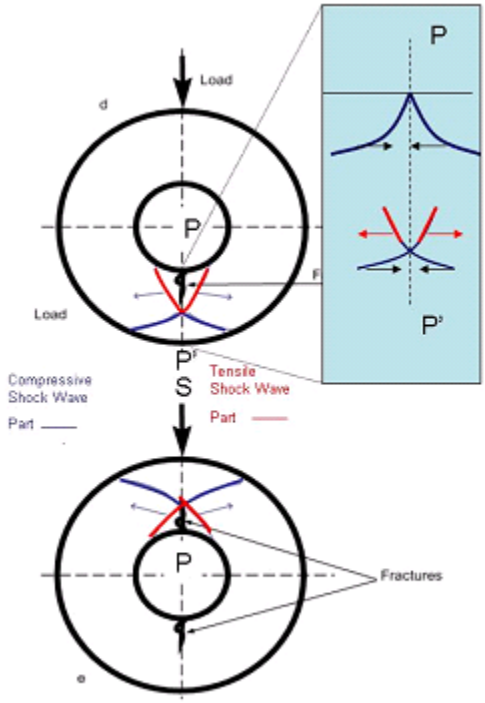

Figure 1-2
Propagation of a shock pulse through the cross section of a tube leading to failures at the internal diameter directly under and opposite to the position of the explosive load. [1]

1.2 Aging Embrittlement

Aging embrittlement to shock loading of T-300 series stainless steels occurs after extended service exposure and is a major contributor to explosive cleaning tube failures. The objective of this study is to determine the mechanisms controlling aging embrittlement and to determine how explosive loading parameters and service environment parameters, including Cumulative Collateral Damage (CCD) and explosive cleaning damage, contribute to the aging embrittlement phenomena.

This study focuses on three materials, Types 304H, 321H, and 347H stainless steels. The majority of experimental tube materials in this study have been removed from operating commercial power plant heat exchangers and have varying and unknown service exposures. It is for this reason that materials throughout the report are classified as "new," meaning the material is in the as-received condition from the mill or, "in-service aged," meaning the material has been removed from an operating boiler. Chemical compositions of 304H, 321H, and 347H stainless steels are given in Table 1-1 below.

Table 1-1
Chemical Composition of 300 Series Stainless Steels [2, 3, 4].

Grade	C	Cr	Ni	Mn	S	P	Si	Ti	Nb	Fe
304H	0.04-0.10	18.0-20.0	8.0-11.0	< 2.0	< 0.030	< 0.040	< 0.75	-	-	Bal.
321H	0.04-0.10	> 17.0	9.0-12.0	< 2.0	< 0.030	< 0.040	< 1.00	< 0.60	-	Bal.
347H	0.04-0.10	17.0 – 20.0	9.0-13.0	< 2.0	< 0.030	< 0.040	< 1.00	-	0.32-1.00	Bal.

Preliminary research suggests that in-service aged materials respond differently to shock loading than new tube material causing unexpected failures during explosive cleaning operations. However, these differences have not yet been quantified.

Literature exists concerning high strain rate deformation in many materials. Most studies focus on high pressure (<35 GPa) impact by a metal slug. The deformation mechanisms at these pressures are drastically different than those operating during the explosive cleaning process as well as those operating during quasi-static loading conditions. Explosive cleaning can cause deformation by pressures typically in the range of 10 to 15 GPa which represents the transition from quasi-static deformation mechanisms to shock pressure deformation mechanisms. For comparison, the quasi-static yield and ultimate strengths for Type 304H stainless steel are 205 and 520 MPa [2]. Shock loaded type 304 stainless steels generally result in deformation twinning and dislocation tangles at shock pressures above 15GPa. At lower pressures, stacking faults and dislocations generally arise. Shock loading subjects materials to strain rates on the order of 10^5 - 10^6 s^{-1} which results in dislocation densities of approximately 10^{15} - 10^{16} m^{-2}, which are considerably higher than that obtained after quasi-static deformation to similar strains [5]. Type 347 stainless steel reacts to shock loading in a manner similar to that of type 304. Explosive cleaning conditions, therefore, allow almost all possible deformation mechanisms to occur during explosive cleaning. Furthermore, attenuation of the shock pressure as the pulse travels

through the tube material allows for a gradient of deformation behavior that is described later in this report. The following section provides an overview of deformation mechanisms in T-300 series austenitic stainless steels.

2
DEFORMATION IN AUSTENITIC STAINLESS STEEL

2.1 Factors Affecting Deformation Mechanism

Many factors influence the behavior of the material under shock loading. These parameters are represented by three categories: material, explosive, and environmental parameters. Material parameters include grain size, specimen geometry, and composition, which determines crystal structure, microstructural constituents, and Stacking Fault Energy (SFE). Shock parameters arise from the properties of the explosive, slug or laser used to initiate the shock front. Shock parameters include pressure pulse shape, detonation or shock velocity, and the orientation of the explosive charge in relation to the tube surface.

When a stick of dynamite is oriented parallel to the surface of a tube the shock wave interacting with the tube surface can be approximated as a plane wave; when the dynamite is oriented normal to the surface of a tube, the shock front has a spherical geometry. Different loading geometries, such as the two cases above and those in between, referred to as oblique, produce different evidences in the form of plastic deformation, and in extreme cases microstructural variation. For example, in low SFE materials, a plane wave shock above the critical twinning pressure favors the formation of microtwins as opposed to microbands [6]. Furthermore, ambient temperature is the major environmental parameter that influences stacking fault energy which increases with increasing temperature [7]. Pressure pulse shape encompasses the stress pulse amplitude, pulse duration, number of periods and decay of the pulse.

2.2 Deformation Mechanisms in Austenitic Stainless Steel

Several deformation mechanisms exist for shock loaded austenitic stainless steel. The deformation mechanisms are: dislocation motion by cross-slip, shear banding, deformation twinning, microband formation and martensite transformation.

2.2.1 Dislocations

Even though low SFE materials have been shown to deform primarily by slip of planar arrays of dissociated partial dislocations, cross-slip can occur for non-planar shock deformed materials [9]. Figure 2-1 shows a bright field TEM micrograph of dislocations in 304L stainless steel with an arrow pointing to dislocation loop source.

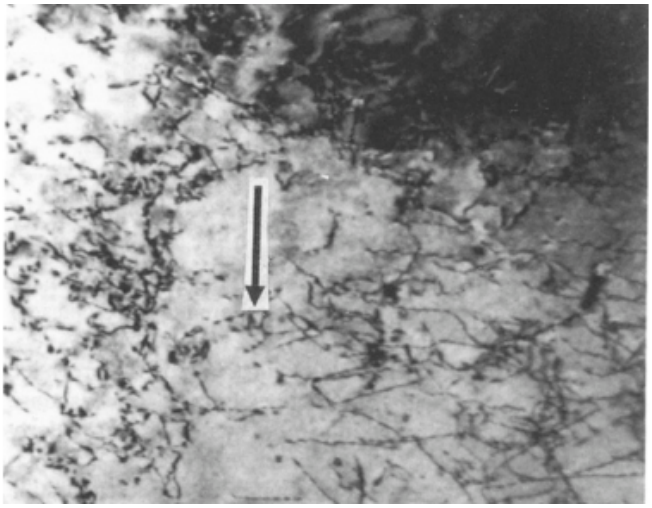

Figure 2-1
Evidence of dislocation loop in polycrystalline iron. [8]

2.2.2 Shear Band

The formation of localized shear bands occurs on (111) planes in FCC metals including T 300 series stainless steel as a result of dislocations developing in planar arrays on many (111) planes. Figure 2-2a is an image of a macroscopic shear band whereas Figure 2-2b is of microscopic shear bands intersecting [9]. The difference between the two scales of shear deformation lies in that microscopic shear banding cannot be evidenced at the macroscopic level and that macroscopic shear bands are composed of enough microscopic shear bands such that they can be viewed with optical imaging techniques.

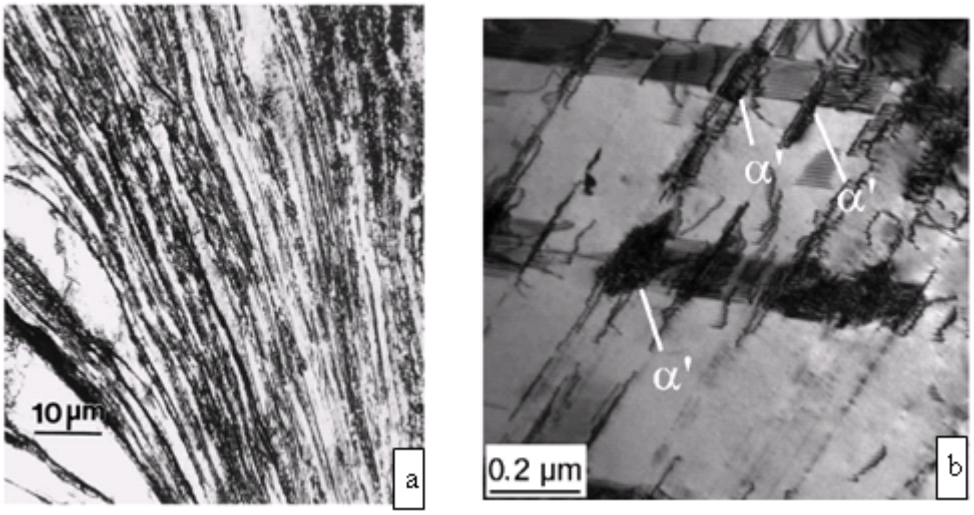

Figure 2-2
Macroscopic shear band in austenitic stainless steel (a); intersection of microscopic shear band in austenitic steel with martensite at the location of intersection. [10]

2.2.3 Martensite

Within shear bands and especially the intersection of shear bands there is a possibility of transforming austenite to a highly faulted α' martensite. However, shear banding adiabatically heats the shocked metal which suppresses the martensite transition [11].

Additionally, martensitic transformation is the predominant deformation mechanism at low strain rates for moderate strains (above 5 pct.) and is aided by low temperatures. Two forms of martensite are present in austenitic stainless steels. These are α' (bct) and ε (hcp) martensite. α' forms at low strain rates, in shear bands and at twin and also ε martensite intersections. ε also forms at very high shock pressures (typically above 35 GPa) [12]. Figure 2-3 shows the morphology of α' (bct) and ε (hcp) martensite.

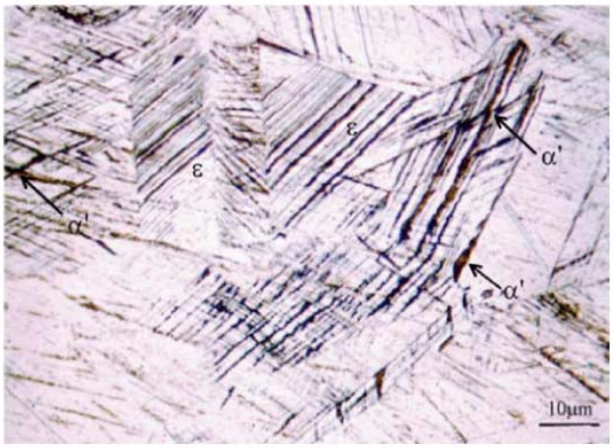

Figure 2-3
Microstructure of 304 stainless steel strained to 10% at -50°C exhibiting both α' and ε martensite. [6]

2.2.4 Twins

Deformation twins have boundaries comprising stacking fault partials on (111) planes due to the materials inability to cross-slip at the given deformation conditions. Inability to cross-slip is caused by a low SFE (less than 20 mJ/m^2). Figure 2-4 is a TEM micrograph of deformation twinning in 304 stainless steel. [6]

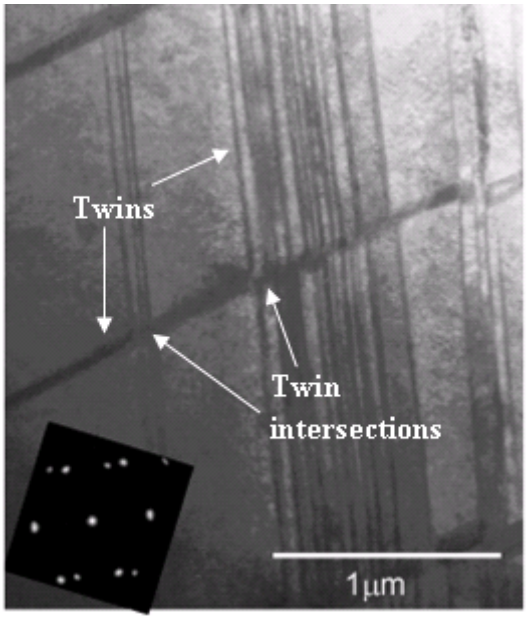

Figure 2-4
Deformation twins in austenitic stainless steel produced by shock loading. [12]

2.2.5 Microbands

Although twinning is predicted for low SFE materials above a critical twinning pressure (CTP), microbands can be present in material that has been subjected to a non-planar shock [9]. Microband boundaries are dislocation double walls created by dislocations coincident with (111) planes. Microbands appear similar in morphology to twins in the optical microscope because they occur on the same slip system but the boundaries are not as uniform. Additionally the misorientation between the microband and the parent crystal is typically two to three degrees whereas the misorientation between twins and their parent crystal is 60 degrees. Finally, microbands have a boundary spacing of 200-300 nm while twin boundary spacing is 20-30 nm. It is for the preceding reasons that these features are easily distinguishable in TEM micrographs. Figure 2-5 shows a TEM micrograph of a microband in 304 stainless steel.

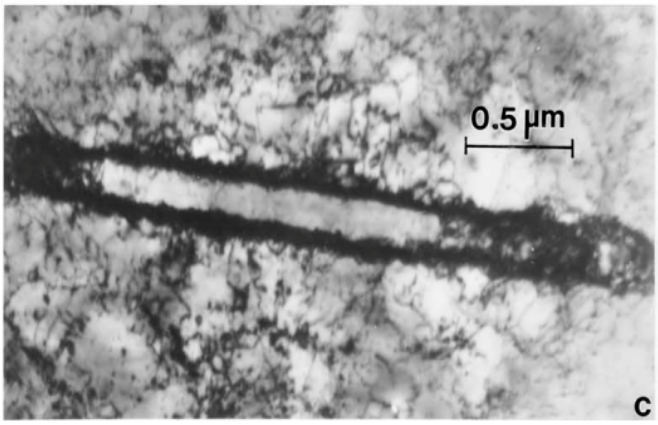

Figure 2-5
Microband in austenitic stainless steel showing the dislocation double wall with a relatively strain free region inside the cell. [6]

2.3 Baushinger Effect

The Bauschinger effect describes the reversal of dislocation motion upon the unloading cycle which does not generate dislocation line length whereas cross-slip, an expected deformation mechanism does. Materials exhibiting low SFE favor the reversal of dislocation motion on slip planes over cross-slip. Since dislocation line length is related to strength increase, work hardening is retarded and dislocation density is expected to be lower than expected from current models in low SFE materials [5].

3
EXPERIMENTAL DESIGN

Several experiments were designed to determine the factors affecting material response to blasting under a wide range of conditions. Variables tested include: charge amount, stand-off distance, whether or not tubes are covered in slag, slag thickness, slag mechanical properties, whether or not a tube is filled with water, repeat blasting, geometry of tube (bends), whether a tube has been welded, weld joint type, and material within T-300 series stainless steel. All blasting experiments were carried out at the CSM Explosives research Laboratory (ERL) at the Edgar Mine, Idaho Springs, CO.

3.1 Blast Matrices

Table 3-1–Table 3-3 describe the variables tested in each group of experiments. Table 3-1, Bare tube blasting matrix, shows that five experimental assemblies, each consisting of two T-300 series stainless steel tubes were blasted with charge amounts of either 0.25 lb. or 0.50 lb. UNIMAX Dynamite, with or without stand-off distance. A schematic representation of this experimental setup is given in Figure 3-1. The tube sections in Table 3-2, Weld blasting matrix, consisted of six in. sections of in-service aged Type 347H stainless steel tube material with either a longitudinal or circumferentially oriented weld overlay performed at the Colorado School of Mines (CSM) or a butt welded sample provided by industry. In each test comprising of two tubes one of the tubes is filled with water and the other is left empty. The tubes in each test are either in the as-welded condition or given an additional heat treatment for one hour at 750°C to simulate a short service interval without solutionizing and promoting growth of carbide precipitates and other non-austenitic phases such as sigma phase. Table 3-3, Simulated slag blasting matrix, describes the test used to evaluate the response to blasting of real boiler slag boulders which were affixed to experimental assemblies with anchoring epoxy. The results of these experiments are used to compare the response to blasting of simulated slag by porous, light concrete and by reconstitution and cementing of real boiler coal ash. Schematic representations of the slag boulders affixed with epoxy and light concrete simulated slag and a photograph of the light concrete experiment are shown in Figure 3-2, Figure 3-3, and Figure 3-4, respectively. The slag boulders used in these experiments were machined by Denver Marble Inc. to ensure a snug fit between the tubes and slag to prevent premature failure of the slag due to uneven loading at the mating surface. The tubes were arranged similarly to those used in the bare tube blasting matrix in Table 3-1. In Figure 3-4, the Styrofoam pieces used to simulate slag porosity can be seen as well as multiple fractures emanating from the blast crater. The concrete and Styrofoam were distributed in layers to simulate layered slag formation in boilers based on analysis of the slag boulders used in blasting of the epoxied slag boulders. The Styrofoam pieces were used to approximate the size and volume distribution of porosities in the real slag boulders determined by image analysis.

Table 3-1
Bare tube blasting matrix.

Test ID	Material	Number of Tubes			Planned Blasting			
		Water Filled	Empty	Total	Repetitions	Charge amt. (lbs.)	Charge type	Standoff (in.)
10-304-1	New 304H	1	1	2	1	0.25	Dynamite	0
10-304-2	AR 347H	1	1	2	1	0.50	Dynamite	0
10-304-3	AR 347H	1	1	2	1	0.25	Dynamite	0
10-304-4	AR 347H	1	1	2	1	0.25	Dynamite	2
10-304-5	AR 347H	1	1	2	1	0.25	Dynamite	4

Table 3-2
Weld blasting matrix. All tests used 0.5 lbs UNIMAX Dynamite.

Test ID	# of Tubes	Material	Weld Type	Condition of Welded Tubes in Test
10-Weld-347-6	2	AR 347H – CSM Generated welds	Surfacing – Bead on Tube-Circumferential	One water-filled, as-welded; one empty, as welded;
10-Weld-347-7	2	AR 347H – CSM Generated welds	Surfacing – Bead on Tube-Circumferential	One water-filled, annealed; one empty, annealed;
10-Weld-347-8	2	AR 347H – CSM Generated welds	Surfacing – Bead on Tube-Longitudinal	One water-filled, as-welded; one empty, as welded;
10-Weld-347-9	2	AR 347H – CSM Generated welds	Surfacing – Bead on Tube-Longitudinal	One water-filled, annealed; one empty, annealed;
10-Weld-347-10	2	AR 3XXH – Industry Generated Weld	Multipass Butt Joint	One water-filled, as-received; one empty, as-received;

Table 3-3
Simulated slag blasting matrix.

Test ID	Material	Slag Preparation Method	# of Tubes		Planned Blasting		
			Water	Empty	Repetitions	Charge Amt. (lbs.)	Charge Type
10-T22-12	2x T22	MicroBeam Slag	0	3	3	0.25	UNIMAX Dynamite
10-3XX-13	2x 321H, 2x AR 347H, 2x New 304H	Light Concrete 7ksi (40 MPa)	3	3	5	0.50	UNIMAX Dynamite
10-3XX-14	2x AR 304H, 2x AR347H, 2x New 304H	Light Concrete 7ksi (40 MPa)	3	3	4	1.00	UNIMAX Dynamite
10-347-15	2x AR 347H	Real Slag Boulders	0	2	2	0.25	UNIMAX Dynamite
10-347-16	2x AR 347H	Real Slag Boulders	0	2	3	0.25	UNIMAX Dynamite
10-347-17	2x AR 347H	Real Slag Boulders	0	2	2	0.25	UNIMAX Dynamite

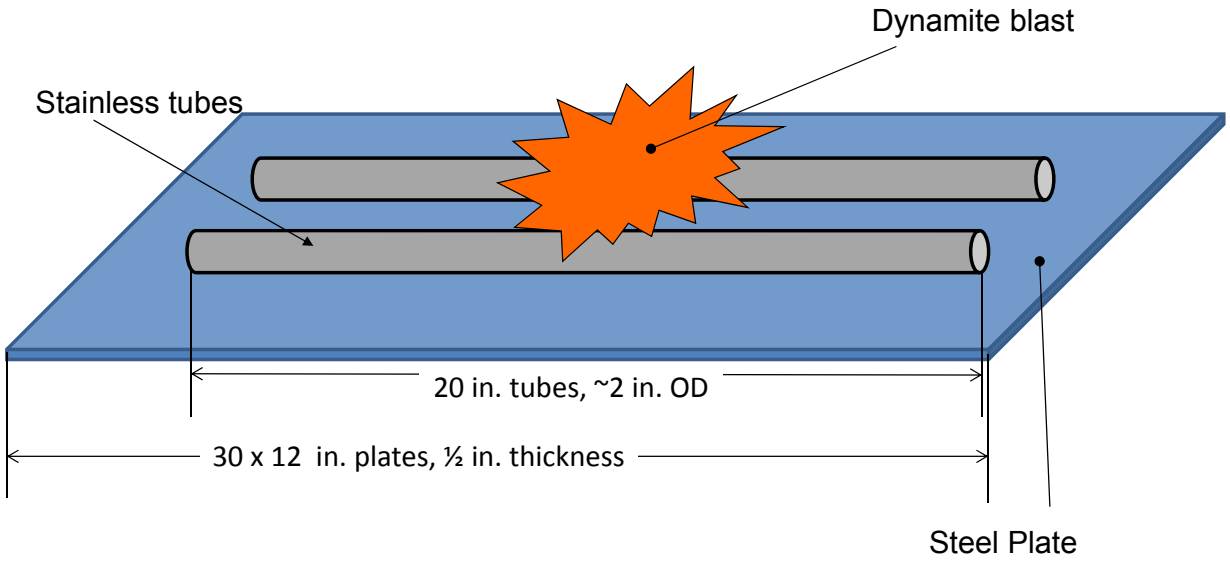

Figure 3-1
Schematic representation of overview bare tube blasting experimental setup indicating location of dynamite blast.

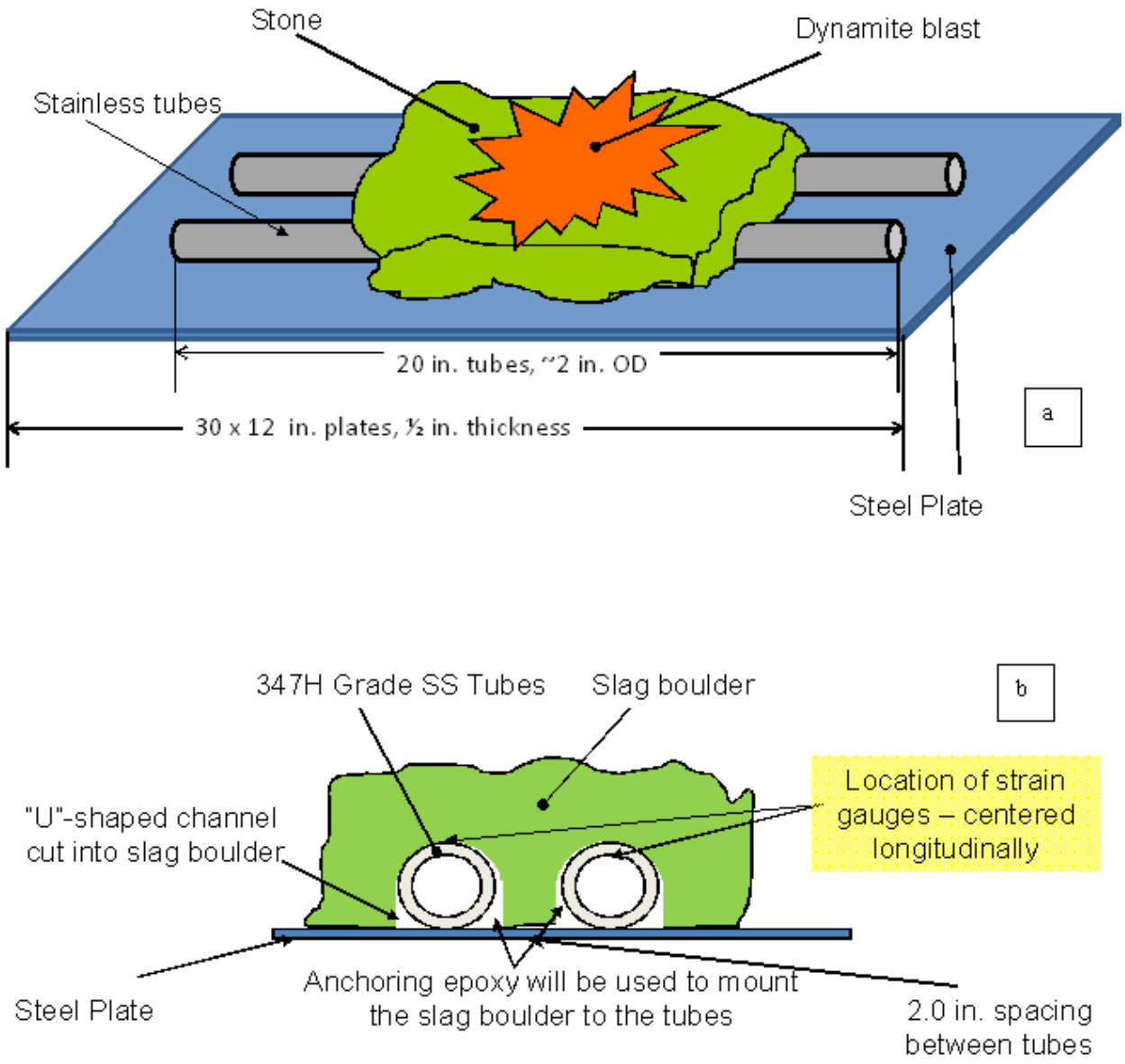

Figure 3-2
Schematic representation of overview (a) and side view (b) of epoxied boiler slag experimental setup showing location of strain gages.

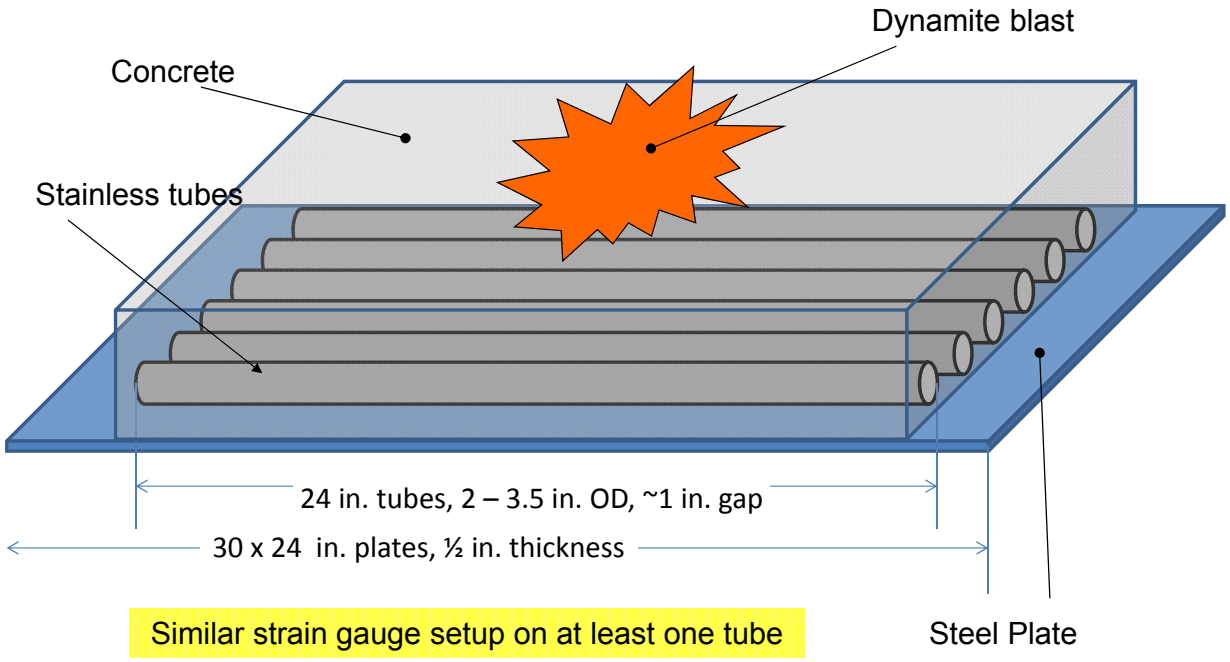

Figure 3-3
Schematic representation of overview of simulated slag by light concrete experimental setup.

Figure 3-4
Photograph of damaged light concrete experimental setup after blasting.

3.2 Instrumentation

Strain gages were attached to the internal diameter (ID) of several tubes in the bare tube and slag blasting matrices by using an applicator tool designed at CSM. The purpose of applying strain gages was to record the shape, amplitude and decay of pressure pulses delivered by the dynamite blasts. Linear strain gages were used to record hoop stress at various locations in the experimental setups. Figure 3-2 shows that the strain gages were applied to either the ID or OD surfaces of a tube, centered and longitudinally oriented at the top of the tube. Recording of the pressure pulses was successful. The data were recorded on a Tektronix TDS 2014 oscilloscope and exported to Microsoft Excel via a cross-over serial connection to a PC. A pair of plots is shown in Figure 3-5. The plots show that the strain experienced by one tube with the real slag boulder experiment and the strain experienced by another tube in a simulated slag by light concrete experiment is similar. The data in both plots are clipped at about 0.10 engineering strain due to the design of the amplifier circuit used to collect the data. Furthermore the pulse shape and attenuation (decay) of the pulse is similar. A series of photographs in Figure 3-6 shows the progression of a real slag boulder experiment with data collection.

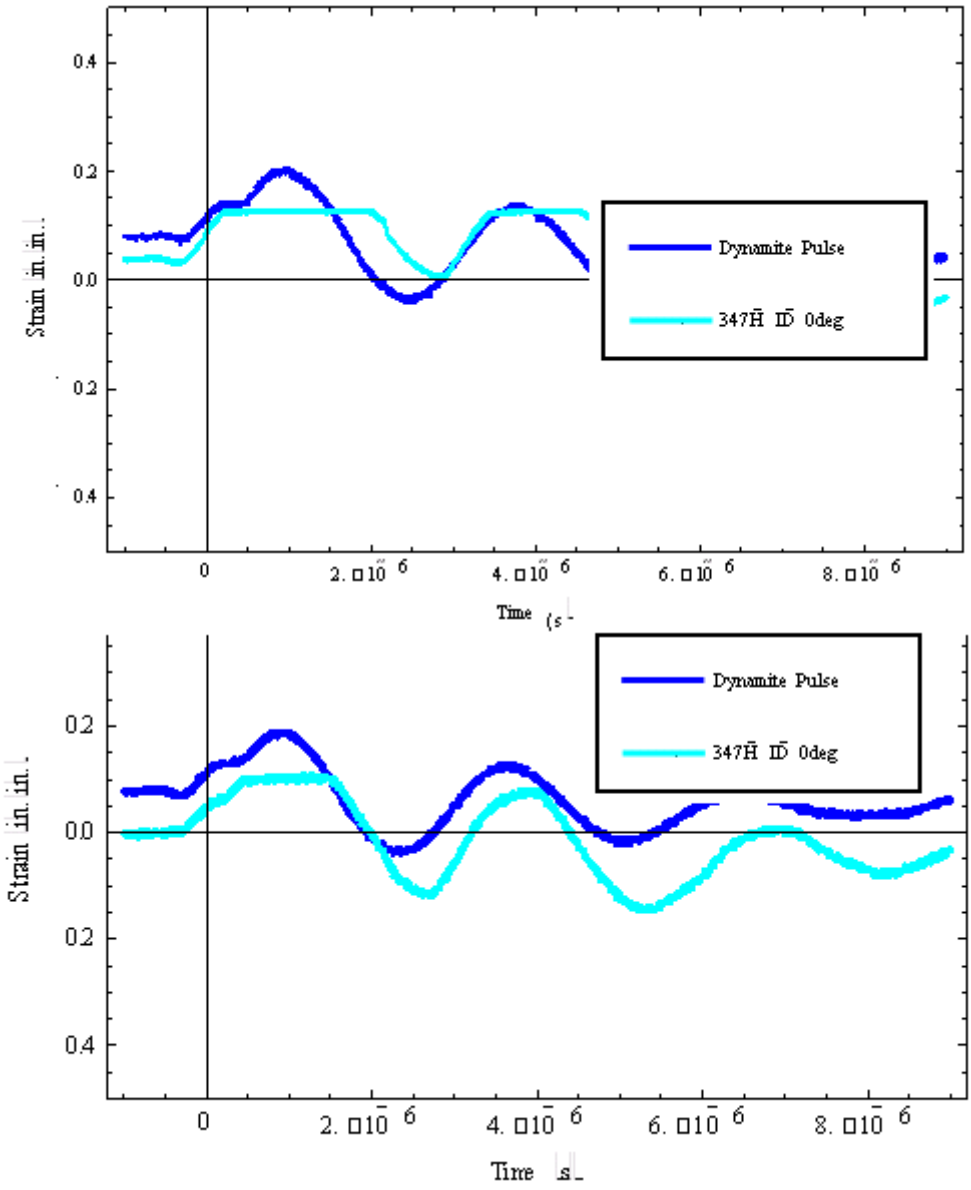

Figure 3-5
Comparison of dynamite pulse and material response for epoxied slag boulder (a) and light concrete simulated slag (b) experiments.

Figure 3-6
Photographs of progression of epoxied slag boulder experiment showing data collected on an oscilloscope.

4
MATERIAL CHARACTERIZATION

Microhardness traverses indicate that the shock pulse affects the mechanical properties closer to the ID and OD surfaces of the tube as compared with the tube wall interior. Figure 4-1 shows a plot of microhardness traverses for the three tube profiles in 304H stainless steel tube material: 304-New-bm, a new tube with no blasting experience; 304-A-bm, an in-service aged tube with no experience, and 304-ii-0deg-bm; the same in-service aged tube after blasting five times with 1.0 lb. charges for a total of 5.0 lbs. of UNIMAX Dynamite. The stand-off distance varied from 6 in. during the first blast to about 3 in. by the final blast which changed the blast intensity which was measured with strain gages. Although there is no noticeable deformation in the tube the mechanical properties have been affected.

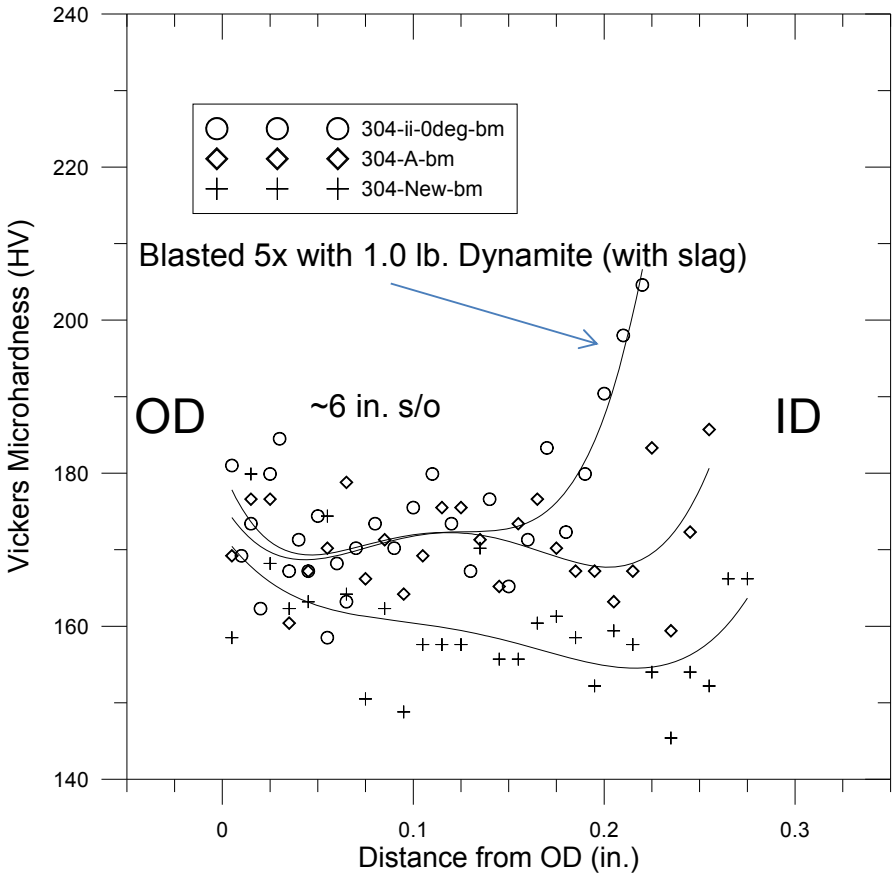

Figure 4-1
Microhardness traverses comparing new tube material with in-service aged and in-service aged and blasted tube materials.

Figure 4-2 shows that microhardness increases strongly as a function of stand-off distance. In the plot, the lowest three microhardness traverses are the same as presented in Figure 3-5. Comparing traverses of samples blasted once each with the same charge amount (1.0 lb) or less (0.75 lb.) with no stand-off distance shows that the blast wave is greatly attenuated by the slag material. Tube samples 304-2-0deg-bm and 304-4W5-0deg-bm suffered considerable plastic deformation. Shock induced mechanical twinning was discovered in these samples, However it was confined to the OD surface of the tube.

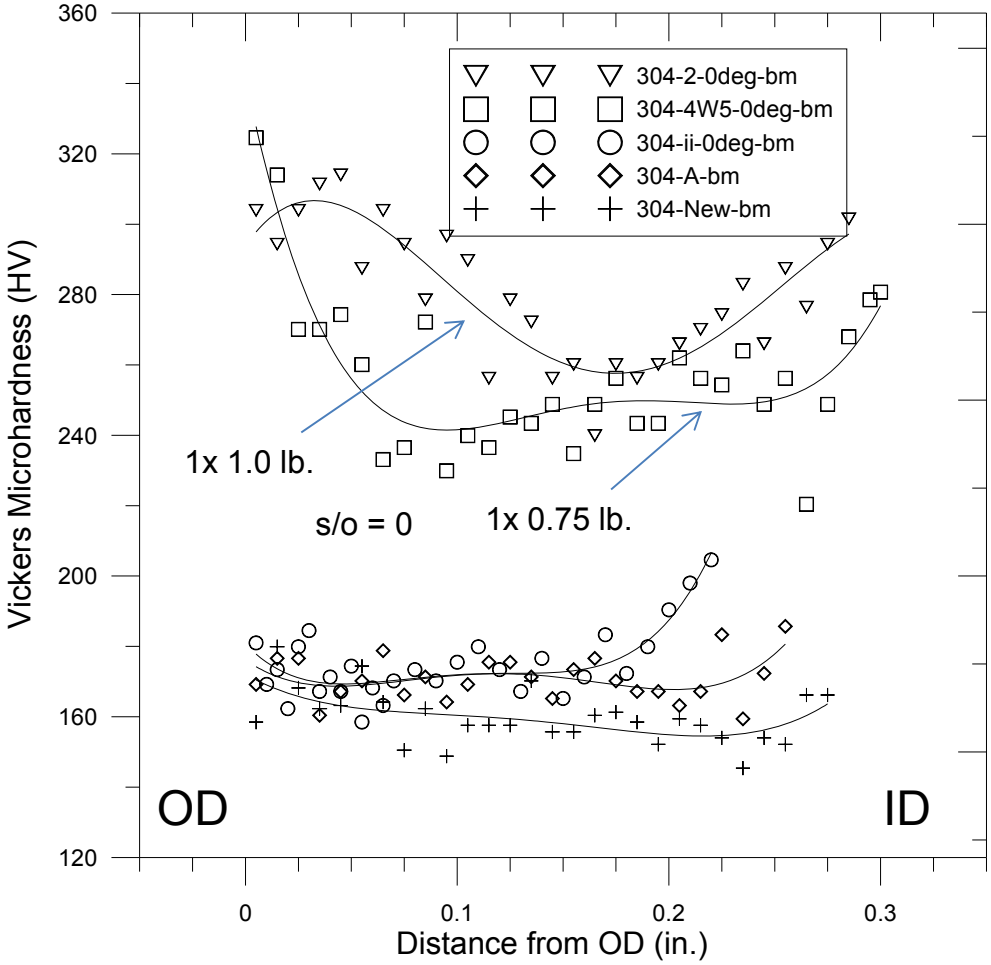

Figure 4-2
Microhardness Traverses of 304H stainless steel tubes having various blasting exposure.

Micro hardness traverses of weld metal as compared to base metal are presented in Figure 4-3. It is shown that weld metal behaves similarly to base metal despite having dissimilar microstructure. The traverses were taken down the centerline of the weld deposit from OD to ID. A schematic showing the location of the Microhardness traverses is given in Figure 4-4. As in the previous plot the lower hardness traverses were taken in a tube blasted five times with 1.0 lb. charges of dynamite through several inches of simulated slag and the higher hardness traverses were taken in a tube blasted with a 0.75 lb. charge of dynamite with no stand-off distance. Weld metal did not show evidence of mechanical twinning. TEM analysis of deformation substructure

will be performed on new and in-service tubes with and without blasting exposure and welding to determine the dominant deformation mechanisms at various depths from within the wall thickness of a given tube.

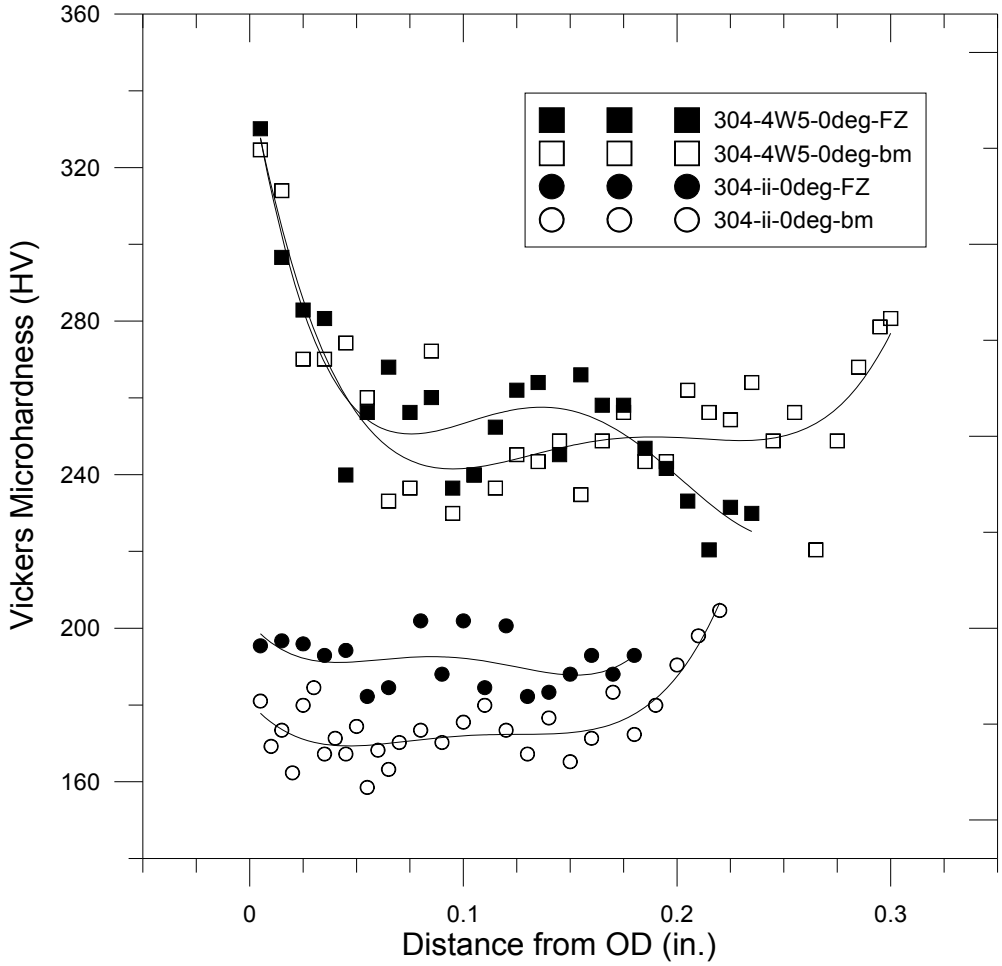

Figure 4-3
Microhardness Traverses of 304H stainless steel base metal and weld metal tubes having different blasting exposure.

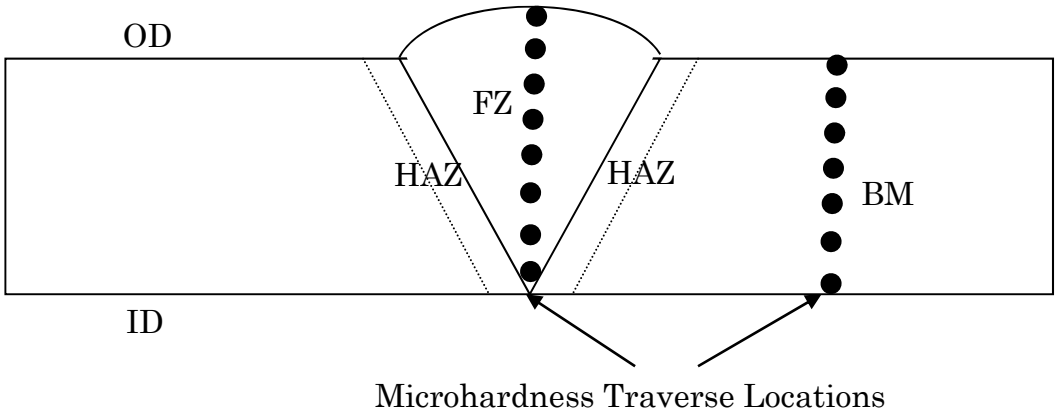

Figure 4-4
Schematic of longitudinal view of welded tube butt joint indicating the locations of fusion zone (FZ) and base metal (BM) microhardness traverse locations.

Metallographic analysis was performed on blasted welded sections and revealed that non austenitic phases existed outside of the fusion zone of the weld deposit. Sigma phase formation in austenitic stainless steels can lead to material embrittlement. Sigma phase is a non-magnetic intermetallic phase composed of iron and chromium which forms at temperatures of 560-980°C. Sigma phase typically has either a needle-like morphology if it is formed within grain interiors or a blocky morphology if it is formed along grain boundaries. It causes loss of ductility and toughness at lower temperatures and detrimental to creep properties. Sigma phase will form preferentially at higher concentration of chromium and lower concentrations of nickel, thus the common 18-8 stainless steels are susceptible to sigma embrittlement [13]. The formation of carbon depletion zones around metal carbides also increases the probability of sigma formation in high chromium steels.

Optical micrographs of this non-austenitic phase are shown in Figure 4-5 and Figure 4-6. The fusion line of a welded tube is near the top left corner of the micrograph in Figure 4-5. The micrograph in Figure 4-6 is an enlargement of the region inscribed by the blue rectangle in Figure 4-5 and shows the blocky morphology of this phase which is found primarily at triple points and on grain boundaries.

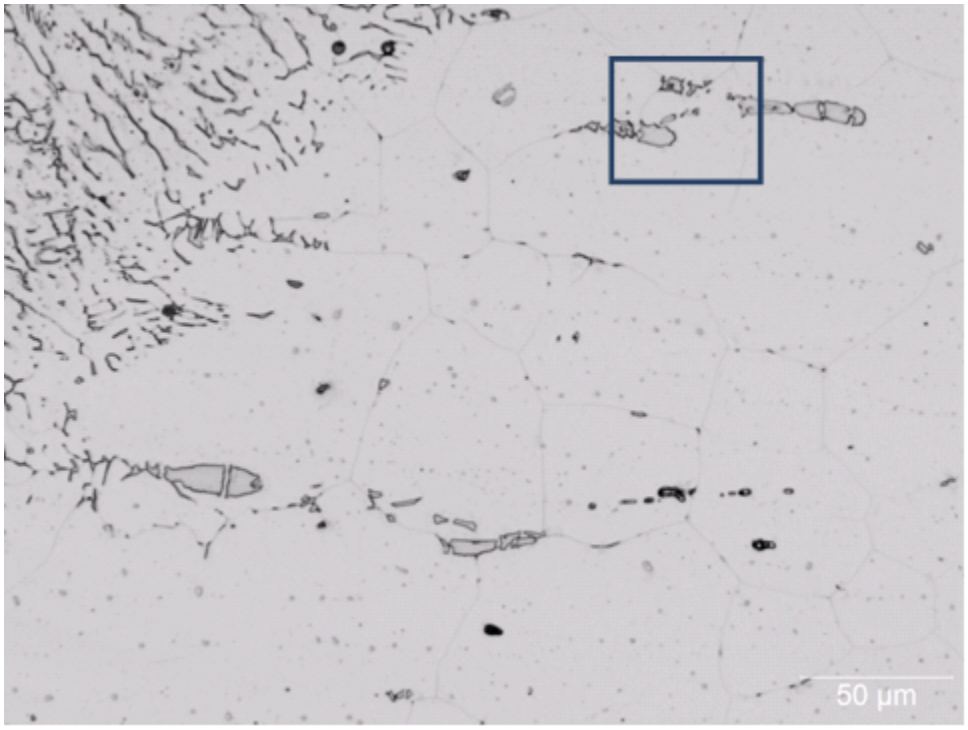

Figure 4-5
Non-austenitic phase protruding into base metal from fusion line.

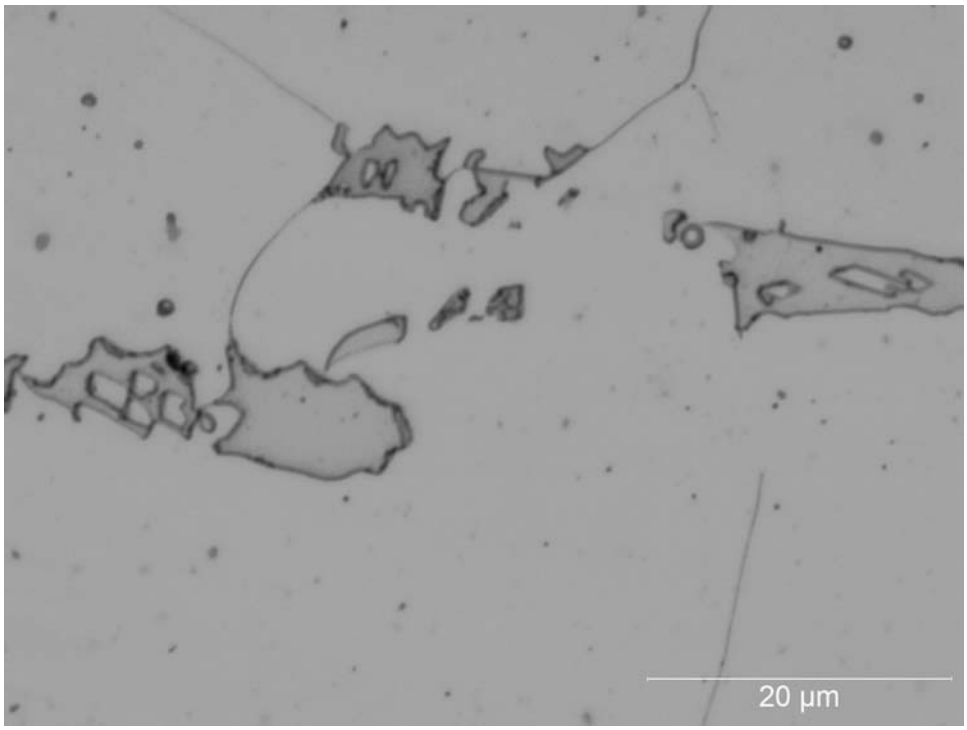

Figure 4-6
Enlargement of non-austenitic phase protruding from fusion line showing morphology.

SEM Backscatter imaging was also used to observe non-austenitic phases near the fusion line in welded and blasted samples. Figure 4-7 is a backscatter electron image (BSEI) near the fusion line in base metal of a 347H tube sample blasted with 0.5 lb. dynamite. Austenite is labeled γ whereas the phase in the optical micrographs in Figure 4-5 and Figure 4-6 is labeled 1 and a different microconstituent is labeled 2. It is likely that phase 1 is sigma phase.

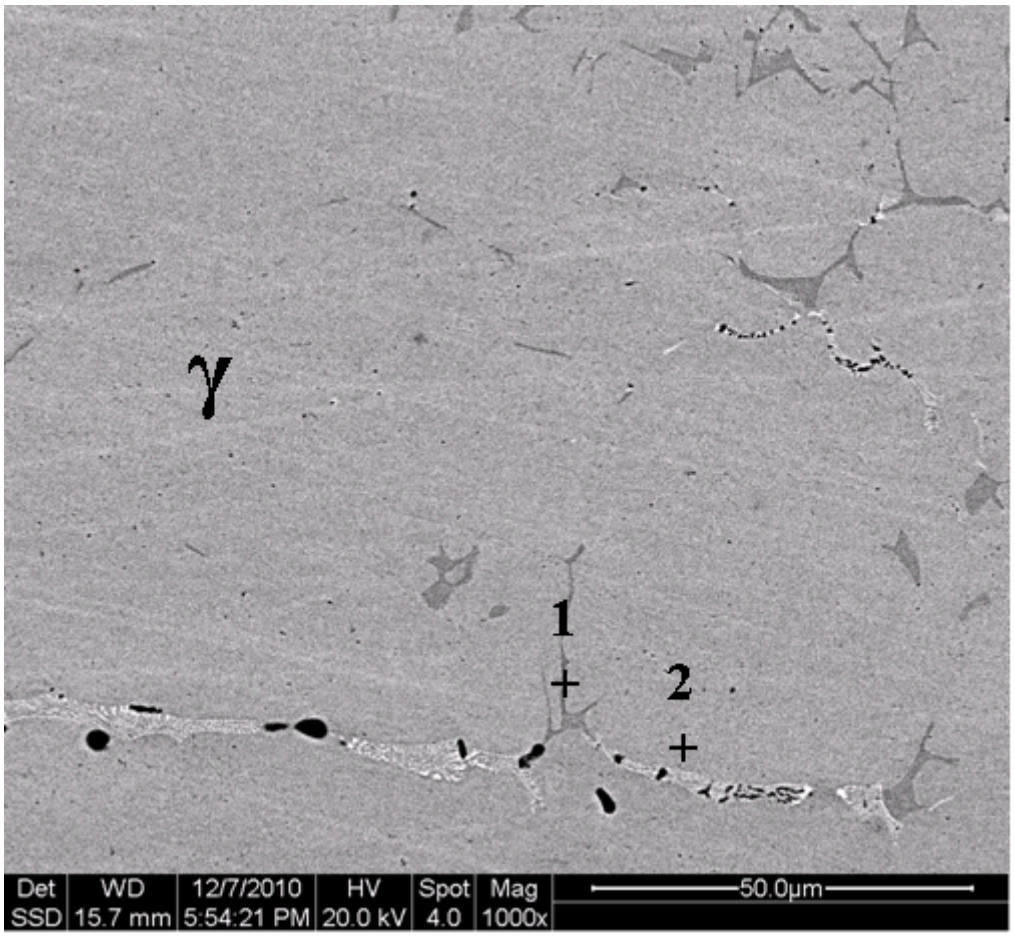

Figure 4-7
BSEI showing austenite, labeled γ, another non-austenitic phase, labeled 1, and another microconstituent, labeled 2.

Higher magnification backscatter electron imaging in Figure 4-8 reveals phase 2 has a lamellar structure and likely has a eutectoid composition. The lamellar microconstituent (2) comprises at least two phases other than the austenite matrix surrounding it. These phases are indicated on the figure as (L) and (D) while the matrix in the immediate area of the lamellar structure is labeled as γ_L. SEM Energy dispersive spectroscopy (EDS) results for the various phases (γ, D, L and γ_L) are presented in Table 5. The compositions of each phase are given in weight percent.

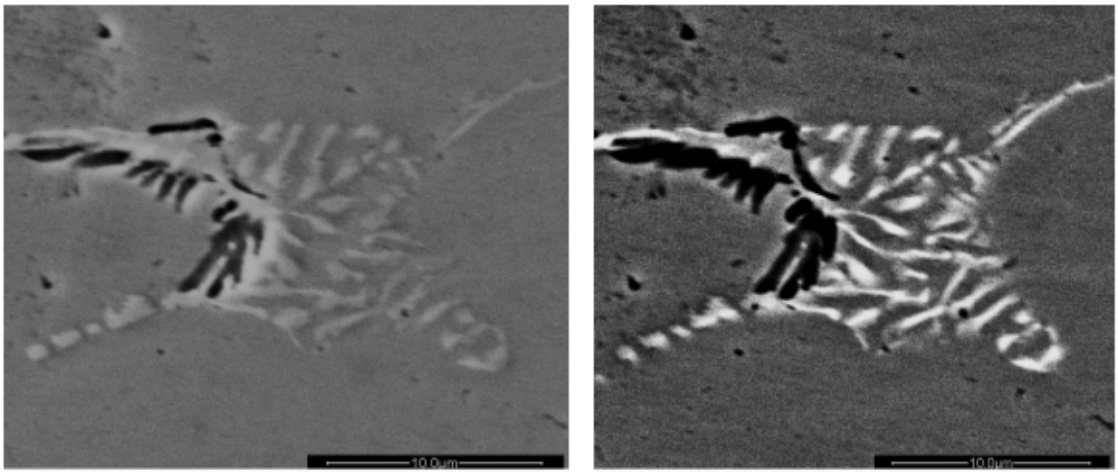

Figure 4-8
SEM micrographs of lamellar structure; a) shows a secondary electron image, evidencing the topography of the structure, while b) is a backscatter electron image of the area.

Table 4-1
Chemical composition of Various phases in Figure 4-8.

Element	γ	1	D	L	γ_L
Si	0.89	0.81	0.66	0.97	0.5
Mn	2.57	2.27	1.43	1.58	1.03
Fe	65.78	67.31	56.67	59.48	65.91
Ni	11.11	4.26	9.43	10.79	10.69
Cr	19.47	24.77	20.55	22.03	21.11
Nb	0	0.46	5.7	5.15	0.76
S	0.18	0.12	5.56		

Phase 1 was found to be enriched in chromium and depleted in Nickel. It was also discovered that the dark phase (D) contained a high sulfur concentration of about 5.5 wt % indicating that these lamellar structures could have been produced in the vicinity of sulfide stringer inclusions. Both the dark phase and light phase (L) contained over 5 weight percent Nb. Phase 1 has morphology similar to that of sigma phase and composition similar to that reported in literature (14). TEM diffraction analysis of the area near the fusion line in the welded samples is needed to confirm these findings.

Even though a considerable amount of non-austenitic phases were formed in the welded samples, the tubes did not fail by brittle fracture indicating that the growth of these phase is not a significant requirement for aging embrittlement in in-service aged T-300 series stainless steel boiler tubes.

5
CONCLUSIONS

Deformation mechanisms in T-300 series austenitic stainless steels have been reviewed. Factors affecting which deformation mechanism operates during explosive cleaning simulation experiments are being evaluated, however the following conclusions can be drawn:

- Shock-induced mechanical twinning predominates near the outer surface of the tube where shock pressures exceed roughly 15 GPa.
- Even though twining is confined to the outer surface of the tube, significant hardness increases can occur throughout the wall thickness after shock loading.
- Using a stand-off distance of at least three inches (including slag thickness) prevents shock-induced mechanical twinning for at least four blasts of 1.0 lb. dynamite and five blasts with 0.5 lb. dynamite in T-300 series stainless steel tubes blasted at the Colorado School of Mines. However, mechanical properties are still significantly affected.
- The strain history caused by blasting has been recorded showing the mechanical response of several tubes to various blast conditions and geometries as well as the decay in amplitude of the pressure pulse. Real slag boulders epoxied onto tube sections attenuate blast pressure similarly to light concrete.
- Several non-austenitic phases were analyzed near the fusion line in the base metal of tubes with weld overlays and butt joints. The growth of these phases did not significantly weaken the austenite matrix and cause pre mature brittle failure. The fusion zone, heat affected zone and base metal performed similarly and showed similar trends in increase in hardness throughout the wall thickness.

6
REFERENCES

1. V. Petr, S. Liu, D. L. Olson, J. C. Madeni, C. Trickel and R. Hellner, “Explosive Cleaning Boiler Tube Damage Mitigation” EPRI Report, CSM Project: MT-CWJCR-010-002.
2. AISI 304H Stainless Steel, Austenitic, http://www.matweb.com/search/DataSheetDataSheet.aspx?MatGUID=f6db3911a2bd463bbb67637c5685a5c1&ckck=1, Accessed 7 Oct 2010.
3. AISI 321H Stainless Steel, Austenitic, http://www.matweb.com/search/DataSheet.aspx?MatGUID=e78890fd8b1e48a7b0ceb9be0330e9e7&ckck=1, Accessed 7 Oct 2010.
4. AISI 347H Stainless Steel, Austenitic, http://www.matweb.com/search/DataSheet.aspx?MatGUID=2f6856f02bcd4379b6465989afa3a85b, Accessed 7 Oct 2010.
5. A. Rohatgi, K.S. Vecchio, The variation of dislocation density as a function of the stacking fault energy in shock-deformed FCC materials, Materials Science and Engineering A328 (2002) 256–266.
6. L.E. Murr, in Shock Waves and High Strain Rate Phenomena in Metals, M.A. Meyers and L.E. Murr, eds., Plenum Press, New York, NY, 1981, pp. 753-77.
7. R. M. Latanision, A. W. Ruff Jr., The Temperature Dependence of Stacking Fault Energy in Fe-Cr-Ni Alloys, Metallurgical and Materials Transaction B Vol. 2 Num. 2, 1971, pp 505-509.
8. EA. Khalid, D.V. Edmonds, and B.D. Goldthorpe, A TEM Study of Deformation Substructure in High Strain Rate and Explosively Shock-Loaded Polycrystalline Iron, JMEPEG (1996) 5:23-26.
9. L. E. Murr, E. V. Esquivel, Review: Observations of common microstructural issues associated with dynamic deformation phenomena: Twins, microbands, grain size effects, shear bands, and dynamic recrystallization, Journal of Material Science vol. 39, (2004) pp 1153-1168.
10. Juho Talonen, Pertti Neonen, Gersom Pape, and Hannu Hanninen, Effect of Strain Rate on the Strain-Induced gamma to alpha prime-Martensite Transformation and Mechanical Properties of Austenitic Stainless Steels, Metallurgical and Materials Transactions A Vol. 36A, February 2005 pp 421.
11. Amar K. De, David C. Murdock, Martin C. Mataya, John G. Speer, David K. Matlock, Quantitative measurement of deformation-induced martensite in 304 stainless steel by X-ray diffraction, Scripta Materialia 50 (2004) 1445–1449.

12. B.H. Sencer, S.A. Maloy, and G.T. Gray III, The Influence of Explosive-Driven Shock Prestraining at 35 GPa and of High Deformation on the Structure/Property Behavior of 316 L Austenitic Stainless Steel, Metallurgical and Materials Transactions A Vol. 36A, July 2005—1825.
13. Hau, J. and Seijas, A. "Sigma Phase Embrittlement of Stainless Steel in FCC Service." NACE Conference . Houston TX: NACE International, 2006.
14. Marián Vach, Terézia Kuníková, Mária Dománková, Peter Ševc, Ľubomír Čaplovič, Peter Gogola, Jozef Janovec, "Evolution of secondary phases in austenitic stainless steels during long-term exposures at 600, 650 and 800 °C." Materials Characterization, (2008): 1792-1798.

Export Control Restrictions

Access to and use of EPRI Intellectual Property is granted with the specific understanding and requirement that responsibility for ensuring full compliance with all applicable U.S. and foreign export laws and regulations is being undertaken by you and your company. This includes an obligation to ensure that any individual receiving access hereunder who is not a U.S. citizen or permanent U.S. resident is permitted access under applicable U.S. and foreign export laws and regulations. In the event you are uncertain whether you or your company may lawfully obtain access to this EPRI Intellectual Property, you acknowledge that it is your obligation to consult with your company's legal counsel to determine whether this access is lawful. Although EPRI may make available on a case-by-case basis an informal assessment of the applicable U.S. export classification for specific EPRI Intellectual Property, you and your company acknowledge that this assessment is solely for informational purposes and not for reliance purposes. You and your company acknowledge that it is still the obligation of you and your company to make your own assessment of the applicable U.S. export classification and ensure compliance accordingly. You and your company understand and acknowledge your obligations to make a prompt report to EPRI and the appropriate authorities regarding any access to or use of EPRI Intellectual Property hereunder that may be in violation of applicable U.S. or foreign export laws or regulations.

The Electric Power Research Institute Inc., (EPRI, www.epri.com) conducts research and development relating to the generation, delivery and use of electricity for the benefit of the public. An independent, nonprofit organization, EPRI brings together its scientists and engineers as well as experts from academia and industry to help address challenges in electricity, including reliability, efficiency, health, safety and the environment. EPRI also provides technology, policy and economic analyses to drive long-range research and development planning, and supports research in emerging technologies. EPRI's members represent more than 90 percent of the electricity generated and delivered in the United States, and international participation extends to 40 countries. EPRI's principal offices and laboratories are located in Palo Alto, Calif.; Charlotte, N.C.; Knoxville, Tenn.; and Lenox, Mass.

Together…Shaping the Future of Electricity

1022240

Electric Power Research Institute
3420 Hillview Avenue, Palo Alto, California 94304-1338 • PO Box 10412, Palo Alto, California 94303-0813 • USA
800.313.3774 • 650.855.2121 • askepri@epri.com • www.epri.com